Applied Physics Express 7, 052001 (2014)
http://dx.doi.org/10.7567/APEX.7.052001

Groove-structured metasurfaces for modulation of surface plasmon propagation

Zhengji Xu[1], Tao Li[2]*, Dao-Hua Zhang[1]*, Changchun Yan[3], Dongdong Li[1], Landobasa Y. M. Tobing[1], Fei Qin[1], Yueke Wang[1], Xiaonan Shen[4], and Ting Yu[4]

[1]School of Electrical and Electronic Engineering, Nanyang Technological University, Nanyang Avenue 639798, Singapore
[2]National Laboratory of Solid State Microstructures, College of Engineering and Applied Sciences, Nanjing University, Nanjing 210093, China
[3]School of Physics and Electronic Engineering, Jiangsu Normal University, Xuzhou, Jiangsu 221116, China
[4]School of Physical and Mathematical Sciences, Nanyang Technological University, Nanyang Link 637371, Singapore
E-mail: edhzhang@ntu.edu.sg; taoli@nju.edu.cn

Received February 19, 2014; accepted April 10, 2014; published online April 28, 2014

An alternative metasurface design based on a nonresonant mechanism is proposed and demonstrated. Using the effective medium theory and finite element calculation, we show the relationship between the effective refractive index and the metasurface geometrical parameters, which potentially can be used for tuning the wavelength and wavefront of the surface plasmon polariton (SPP). Experimental studies of our metasurface were conducted by near-field scanning optical microscopy of subwavelength gold grooves fabricated using a focused ion beam (FIB). The metasurfaces give us an alternative method for manipulating SPP propagation. © 2014 The Japan Society of Applied Physics

Surface plasmon polaritons (SPPs) have attracted significant interest for their potential applications in nanophotonic integration,[1–3] sensing,[4,5] biology detections,[6–8] and so on. To date, SPP manipulations using well-defined metallic nanostructures[9–15] have achieved remarkable successes in beam splitting,[16,17] super-resolution imaging,[14] the generation of a hollow beam,[18,19] and sub-wavelength-sized optical devices.[20,21] Recently, there has been growing interest in controlling light using the so-called metasurface,[22] which refers to a type of two-dimensional metamaterial consisting of subwavelength resonant elements. Such a metasurface has shown unique abilities in manipulating light refraction,[22,23] reflection,[24] and even the photonic spin Hall effect with local phase discontinuities, which are considered to beat the conventional Snell's law.[25] Although a similar idea has been proposed to realize the conversion between radiation and surface waves,[26,27] few experiments have been reported on the manipulation of in-plane SPP propagation in the optical region. One possible reason for this is that the metasurface designs are generally resonance-based, which are expected to be highly susceptible to loss and have narrow bandwidth. Therefore, for realizing device performance characteristics that are insensitive to loss within a broad bandwidth, one would need metasurface designs based on a nonresonance mechanism.

The concept of the nonresonant metasurface was initially proposed by Pendry et al.,[28] where artificial electromagnetic surface modes can be supported in structured perfect conductor surfaces. This strategy can be extended to a real plasmonic regime, where the SPP property can be tuned without resonant processes. Instead of employing spoof SPPs based on hole arrays,[28] in this paper, we report metasurfaces designed on the basis of subwavelength grooves in a metal film. The effective medium theory (EMT) is then employed to derive the dispersion relation, which also serves as our design framework, particularly for SPP wavelength modulation. Our numerical simulation shows that the SPP wavelength modulation depends on the structural parameters of our metasurfaces, which is verified experimentally by near-field scanning optical microscopy (NSOM) measurements. We further extend our design to the control of the SPP wavefront, which is also experimentally demonstrated.

The proposed metasurface is schematically shown in Fig. 1(a), which consists of subwavelength grooves perpendicular to the grating coupler used to couple the light from free-space to in-plane SPP waves. As the electric field does not extend in the z-direction, and is tightly confined to the metal surface, the metasurface resembles a case of one-dimensional nanowire arrays. Using EMT of nanowire arrays,[29] the effective permittivity of the metasurface can then be expressed as

$$\varepsilon'_{\text{meta-}x} = \frac{N\varepsilon'_{\text{m}}Q + (1-N)\varepsilon_{\text{d}}}{NQ + (1-N)}, \tag{1}$$

$$\varepsilon'_{\text{meta-}y} = N\varepsilon'_{\text{m}} + (1-N)\varepsilon_{\text{d}}, \tag{2}$$

where $\varepsilon'_{\text{meta-}x}$ and $\varepsilon'_{\text{meta-}y}$ are the effective permittivities for E_x and E_y, respectively, which also coincide with the propagation directions of the SPP in the x- and y-directions. ε_{d} is the permittivity of the dielectric, ε'_{m} is the real permittivity of the metal, $Q = 2\varepsilon_{\text{d}}/(\varepsilon'_{\text{m}} + \varepsilon_{\text{d}})$, and $N = (P-w)/P$ is the metal filling ratio for grooves with periodicity P and width w. Assuming that the groove depth is larger than the SPP penetration depth ($h > \delta_{\text{meta}}$) for the incident light with a wavelength λ_0, we can thus infer the SPP wavelength from a typical SPP dispersion relation,[30]

$$\lambda_{\text{spp}} \cong \lambda_0 \sqrt{\frac{\varepsilon_{\text{d}} + \varepsilon'_{\text{meta-}y}}{\varepsilon_{\text{d}}\varepsilon'_{\text{meta-}y}}}, \tag{3}$$

where the permittivity of metal (ε_{m}) is replaced by $\varepsilon'_{\text{meta-}y}$ for the SPP propagating in the y-direction (which corresponds to electric fields E_y). By substituting Eq. (2) into Eq. (3), the SPP wavelength in a metasurface can be expressed as

$$\lambda_{\text{spp}} \cong \lambda_0 \sqrt{\frac{(2-N)\varepsilon_{\text{d}} + N\varepsilon'_{\text{m}}}{N\varepsilon_{\text{d}}\varepsilon'_{\text{m}} + (1-N)\varepsilon_{\text{d}}^2}} \equiv \lambda_0\alpha, \tag{4}$$

where α denotes the wavelength scaling factor, which is equal to the inverse of the effective index ($\alpha = 1/n_{\text{eff}}$). Table I shows the effective permittivity ($\varepsilon'_{\text{meta-}y}$), effective refractive indices (n_{eff}), and SPP wavelength ($\lambda_{\text{SPP-EMT}}$) derived from EMT for the metasurfaces on a gold film, with the groove periodicity varied from $P = 100$ to 150 nm, and the groove width fixed to $w = 50$ nm, at the incident wavelength $\lambda_0 = 633$ nm.

As a comparison, the E_z field distributions of metasurfaces with the same groove periodicities and groove depth ($h = 50$ nm) were also calculated by the finite element method (FEM) using COMSOL commercial software. The input of the incident electric field is 1 V m^{-1}, and the permittivities are

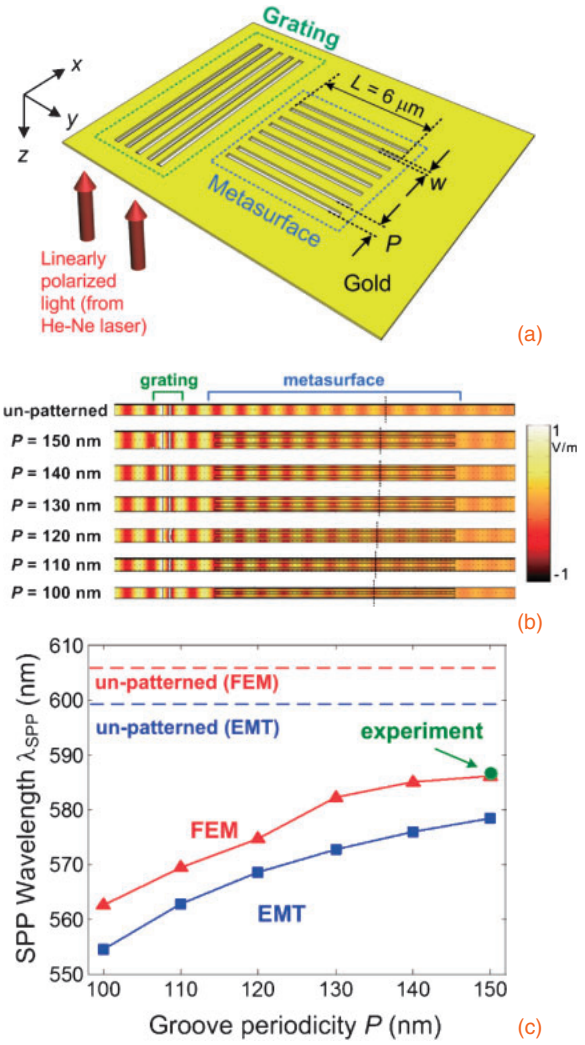

Fig. 1. (a) Schematic of a proposed metasurface formed by an array of 6 μm groves with a fixed period. On its right is a grating coupler. (b) Simulated electrical field intensity distributions E_z in a set of metasurfaces that are formed by grooves with different periodicities but with the same width. The top one is the distribution in a gold film without grooves for comparison. The dashed straight lines indicate the wavefront of the SPP in the metasurfaces, and the wavelength scaling (or shrinking) with decreasing period can be easily seen. (c) SPP wavelengths of metasurfaces in (b), calculated on the basis of EMT (squares) and by FEM (triangles).

$\varepsilon_{Au} = -9.586 + 1.18i$ (for gold) and $\varepsilon_{Air} = 1$ (for air) for the incident wavelength $\lambda_0 = 632.8$ nm.[31] The penetration depth is found to be in the $\delta \sim 30$ nm range, which validates the assumption that the groove depth ($h = 50$ nm) is larger than the SPP penetration depth. The E_z field distribution in a unit cell is shown in Fig. 1(b), where a periodic boundary condition was used and the sparse matrix was solved by using the UMFPACK algorithm. On the other hand, for the large-scale simulations shown in Figs. 2 and 4(b), the scattering boundary condition was used to reduce artificial reflections, and the GMRES algorithm was used to solve the sparse matrix for its rapid convergence. The SPP wavelengths based on FEM calculations are also shown in Table I. The comparison between FEM and EMT is shown in Fig. 1(c), with the case of an unpatterned gold film ($N = 1$) also shown for reference. It can be seen that the EMT results are in qualitative agreement with the FEM results. In general, EMT is very accurate when the structural dimensions are in the deep subwavelength regime ($<\lambda/10$). However, in this work, the groove periodicity of the metasurface is $\sim\lambda/6$, which is not yet in the deep subwavelength range. This may have caused the apparent differences between EMT and FEM results. The second factor contributing to the difference is the fact that only the real part of the gold permittivity is considered in EMT, in contrast to the FEM case that takes into account the complex gold permittivity values. Figure 1(c) shows the geometrical dependence of the SPP wavelength, where the SPP wavelength is shorter for decreasing groove periodicity. This also indicates that the effective refractive index can be increased by decreasing the groove periodicity. This provides us with a framework to design a gradient index (GRIN) metasurface for SPP focusing, as will be shown next.

Table I. Summary of effective permittivity $\varepsilon'_{meta\text{-}y}$, effective refraction index, decay rate of SPP α_{SPP}, SPP wavelengths calculated from EMT of the metasurfaces formed by arrays of grooves with different periods but the same groove width. The SPP wavelengths simulated using the finite element method are listed in the last column for comparison.

P (nm)	N	$\varepsilon'_{meta\text{-}y}$	n_{eff}	α_{SPP} (1/μm)	$\lambda_{SPP\text{-}EMT}$ (nm)	$\lambda_{SPP\text{-}FEM}$ (nm)
	1	−9.586	1	0.2351	599	605.75
150	0.667	−5.987	1.033	0.2519	578.4	586.12
140	0.643	−5.807	1.036	0.2469	575.92	584.98
130	0.615	−5.510	1.04	0.2622	572.69	582.27
120	0.583	−5.172	1.054	0.2829	568.52	574.61
110	0.545	−4.769	1.064	0.2866	562.74	569.37
100	0.5	−4.293	1.077	0.2985	554.39	562.53

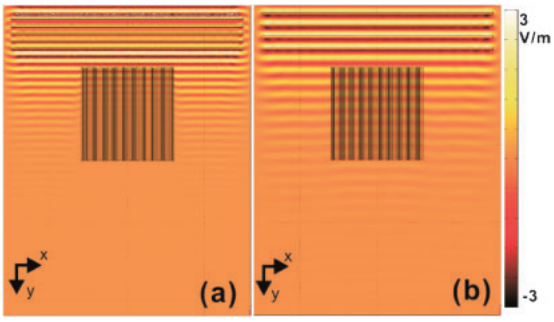

Fig. 2. Calculated E_z field distributions inside and outside the metasurface with an array of $P = 110$ nm grooves at the incidences of (a) 532 and (b) 775 nm.

To investigate this, we simulate electric field distributions of the metasurface illuminated at different λ_0 values, as shown in Fig. 2. It is evident that both $\lambda_0 = 532$ nm [Fig. 2(a)] and $\lambda_0 = 775$ nm [Fig. 2(b)] reveal the wavelength scaling, although the scaling factors are rather different (α is higher for smaller λ_0). This indicates that the metasurface operates under a certain bandwidth, in contrast to the ideal condition where the metasurface characteristics are supposed to be wavelength-independent. We consider that this is due to the fact that the metasurface is treated as a uniform anisotropic medium under the EMT framework, which is valid only if the structures are in the deep subwavelength regime.

The metasurface fabrication was carried out by first sputtering a 210-nm-thick gold film (with a 2-nm-thick Cr

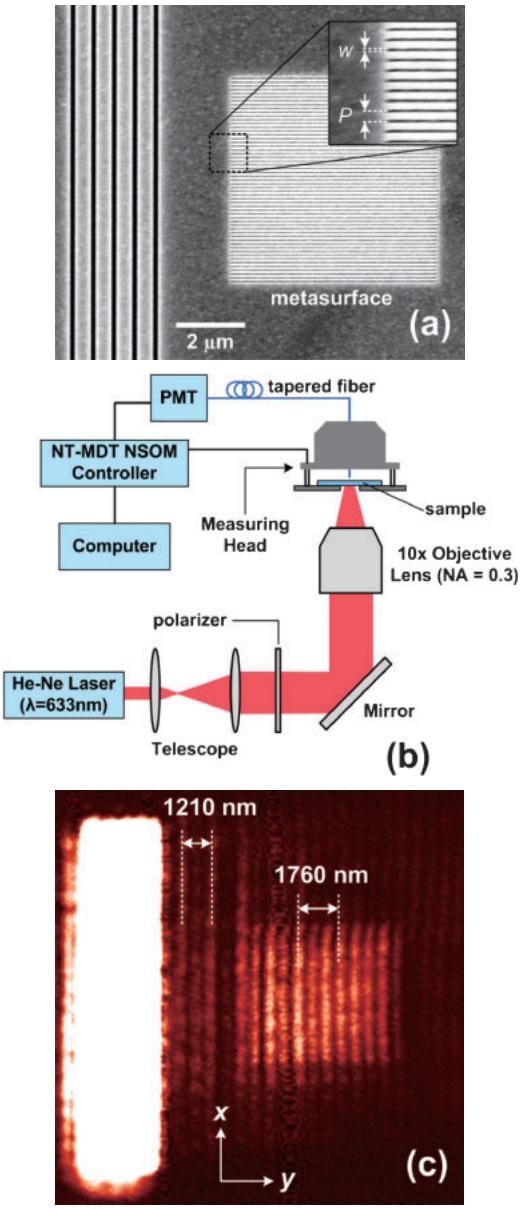

Fig. 3. (a) SEM image of the metasurface formed by an array of grooves with $P = 150$ nm and groove width $w = 50$ nm. (b) Schematic diagram of near-field scanning optical microscope. (c) Measured near-field intensity distribution of metasurface.

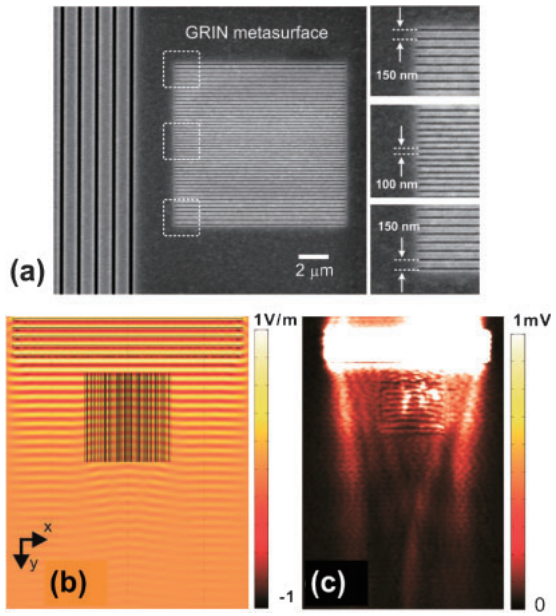

Fig. 4. (a) SEM image of GRIN metasurface formed by grooves with the period progressively decreasing from 150 (at the edge) to 100 nm (at the center). (b) Calculated E_z field distributions of GRIN metasurface. (c) Measured field intensity distribution.

adhesion layer) on a glass substrate, which was followed by metasurface patterning by a focused ion beam (FIB) based on the Ga ion with 30 keV beam energy. The beam currents used for patterning the grating coupler and the metasurface were 20 and 120 pA, respectively. Figure 3(a) shows the fabricated metasurface with the same dimensions as those in the simulation shown in Fig. 1(a), i.e., $L = 6$ μm, $w = 50$ nm, $h = 50$ nm, and $P = 150$ nm. The coupling from free-space to in-plane SPPs is facilitated by the grating coupler [the left grating structure in Fig. 3(a)], which comprises the slit grating with a 15 μm slit length and a 150 nm slit width.

The electric field distributions were characterized using a near-field scanning optical microscope. The characterization setup is schematically shown in Fig. 3(b). The linearly polarized He–Ne laser ($\lambda = 632.8$ nm) was normally incident from the bottom of the glass substrate through an objective lens (Olympus UPlanFLN 10×, NA = 0.3). The aluminium-coated NSOM tip (less than 100 nm in diameter) was positioned about 10 nm from the sample to collect near-field information, which was then amplified by a photomultiplier tube (PMT). The NSOM characterization of the metasurface (for $P = 150$ nm) is shown in Fig. 3(c). Note that there is fringing in the NSOM results, which can be attributed to the interference between the directly transmitted incident beam and the in-plane surface plasmon polariton,[32,33] where the bright (dark) fringes correspond to a constructive (destructive) interference situation. Thus, the SPP wavelengths (λ_{SPP}) can be deduced by measuring the distances between the fringes, i.e., $\lambda_{SPP} = d/(q-1)$, where d is the distance between q fringes. The SPP measured wavelengths are $\lambda_{SPP} \sim 605$ nm ($d = 1210$ nm for $q = 3$) for the unpatterned gold film and $\lambda_{SPP} \sim 586.7$ nm ($d = 1760$ nm for $q = 4$) for the patterned gold film (metasurface). In comparison with our numerical results (see Table I), the measured λ_{SPP} outside the metasurface ($\lambda_{SPP} \sim 605$ nm) is very close to that from FEM calculation ($\lambda_{SPP\text{-}FEM} \sim 605.75$ nm). The measured λ_{SPP} inside the metasurface ($\lambda_{SPP} \sim 586.7$ nm) is also close to the simulated λ_{SPP} ($\lambda_{SPP\text{-}FEM} \sim 586.12$ nm for $P = 150$ nm). The scaling factor can then be deduced by $\alpha = \lambda_{SPP,out}/\lambda_{SPP,in}$, where $\lambda_{SPP,in}$ ($\lambda_{SPP,out}$) is the SPP wavelength inside (outside) the metasurface. Note that the contraction of the in-plane SPP wave can be experimentally observed from the mismatch between inside and outside fringes in Fig. 3(c), thereby validating the theoretical calculation. This also shows, at least indirectly, the tuning of the effective index by introducing subwavelength grooves in a gold film.

Therefore, it is possible to mimic the phase shift in a lens by introducing different effective indices in the lateral direction. This principle is employed to design a GRIN metasurface for in-line SPP focusing. For a fixed groove width, since a shorter groove periodicity gives a higher effective index

[see Fig. 1(c)], the metasurface can approximate the phase response of a lens when the groove periodicity progressively increases from the center to the edge of the metasurface. The fabricated GRIN metasurface is shown in Fig. 4(a), which consists of 56 grooves with the periodicity changed from $P = 150$ (at the edge) to 100 nm (at the center). The groove width is fixed to 50 nm, while the groove periodicity is decreased consecutively for every 2 periods by 5 nm towards the center on the metasurface. The FEM calculation and NSOM results are presented in Figs. 4(b) and 4(c), respectively, where the focusing action can be seen in both cases, showing excellent agreement between them. This is further verified by the fact that the wavefront in Fig. 4(c) is curved instead of straight as in Fig. 3(c), demonstrating that the SPP goes into a lenslike medium. Although such fringes are not phase-resolved as in the FEM calculations shown in Fig. 4(b), we nevertheless have shown a proof-of-concept of SPP focusing by using the GRIN metasurface. Furthermore, we also note that the focusing action in Fig. 4(c) is still considerably weak. A stronger focusing action can be achieved by fabricating denser grooves at the center so as to make the lens exhibit a "stronger index contrast", thus giving a shorter focal length.

We have proposed and demonstrated metasurfaces consisting of subwavelength groove arrays in a gold film, which have been shown to have the capability for wavelength modulation and wavefront engineering. EMT employed in our device design has good agreement with FEM calculations and has been verified by NSOM measurements. In particular, the subwavelength gold grooves with locally varying periodicity have been fabricated and characterized, where SPP wavelength shrinking and in-plane SPP focusing have been experimentally observed. We consider that the proposed metasurface can potentially be used for wavefront engineering, nanophotonics, and metadevices.

Acknowledgments The project is supported by the National Research Foundation (NRF-G-CRP 2007-01), A∗Star (1220703063 and 0921540099), Singapore. T.L. and C.C.Y. acknowledge the National Natural Science Foundation (11174136, 50975187, and 61078019), the Natural Science Foundation (BK2011203) of Jiangsu Province, and the State Key Program for Basic Research (2012CB921501) of China. T.Y. acknowledges the Singapore National Research Foundation under NRF RF award No. NRF-RF2010-07 and MOE Tier 2 MOE2012-T2-2-049. The authors thank Q. Wang, G. Yuan, J. Wang, and L. Du from the School of EEE, Nanyang Technological University, for their help in the NSOM measurement, and B. Cao and C. Qiu from SPMS, Nanyang Technological University, for their assistance in the FIB fabrication. Data are available upon request.

1) D. K. Gramotnev and S. I. Bozhevolnyi, Nat. Photonics **4**, 83 (2010).
2) Y. Fu, X. Hu, C. Lu, S. Yue, H. Yang, and Q. Gong, Nano Lett. **12**, 5784 (2012).
3) P. Fan, C. Colombo, K. C. Y. Huang, P. Krogstrup, J. Nygård, A. Fontcuberta i Morral, and M. L. Brongersma, Nano Lett. **12**, 4943 (2012).
4) K. A. Tetz, L. Pang, and Y. Fainman, Opt. Lett. **31**, 1528 (2006).
5) L. Pang, G. M. Hwang, B. Slutsky, and Y. Fainman, Appl. Phys. Lett. **91**, 123112 (2007).
6) J. R. Lakowicz, Plasmonics **1**, 5 (2006).
7) W. Lukosz, Biosens. Bioelectron. **6**, 215 (1991).
8) L. Y. M. Tobing, L. Tjahjana, D. H. Zhang, Q. Zhang, and Q. Xiong, Sci. Rep. **3**, 2437 (2013).
9) L. Yin, V. K. Vlasko-Vlasov, J. Pearson, J. M. Hiller, J. Hua, U. Welp, D. E. Brown, and C. W. Kimball, Nano Lett. **5**, 1399 (2005).
10) X. Liu, Y. Wang, and E. O. Potma, Appl. Phys. Lett. **101**, 081116 (2012).
11) Y. Luo, J. B. Pendry, and A. Aubry, Nano Lett. **10**, 4186 (2010).
12) L. Li, T. Li, S. M. Wang, C. Zhang, and S. N. Zhu, Phys. Rev. Lett. **107**, 126804 (2011).
13) D. Li, D. H. Zhang, C. Yan, T. Li, Y. Wang, Z. Xu, J. Wang, and F. Qin, Opt. Express **21**, 5949 (2013).
14) L. Li, T. Li, S. Wang, S. Zhu, and X. Zhang, Nano Lett. **11**, 4357 (2011).
15) N. Anttu, Z. Q. Guan, U. Hakanson, H. X. Xu, and H. Q. Xu, Appl. Phys. Lett. **100**, 091111 (2012).
16) C. C. Yan, D. H. Zhang, Y. Zhang, D. D. Li, and M. A. Fiddy, Opt. Express **18**, 14794 (2010).
17) Y. Wang, D. H. Zhang, J. Wang, M. Yang, D. Li, and Z. Xu, J. Opt. **14**, 015103 (2012).
18) C. Yan, D. H. Zhang, D. Li, H. Bian, Z. Xu, and Y. Wang, J. Opt. **13**, 085102 (2011).
19) Z. Xu, D. H. Zhang, C. Yan, D. Li, and Y. Wang, J. Opt. **14**, 114014 (2012).
20) G. Rui, W. Chen, D. C. Abeysinghe, R. L. Nelson, and Q. Zhan, Opt. Express **20**, 19297 (2012).
21) S. Kéna-Cohen, P. N. Stavrinou, D. D. C. Bradley, and S. A. Maier, Nano Lett. **13**, 1323 (2013).
22) N. Yu, P. Genevet, M. A. Kats, F. Aieta, J.-P. Tetienne, F. Capasso, and Z. Gaburro, Science **334**, 333 (2011).
23) A. V. Kildishev, A. Boltasseva, and V. M. Shalaev, Science **339**, 1232009 (2013).
24) S. Sun, K.-Y. Yang, C.-M. Wang, T.-K. Juan, W. T. Chen, C. Y. Liao, Q. He, S. Xiao, W.-T. Kung, G.-Y. Guo, L. Zhou, and D. P. Tsai, Nano Lett. **12**, 6223 (2012).
25) X. Yin, Z. Ye, J. Rho, Y. Wang, and X. Zhang, Science **339**, 1405 (2013).
26) X. Li, S. Xiao, B. Cai, Q. He, T. J. Cui, and L. Zhou, Opt. Lett. **37**, 4940 (2012).
27) Y. Liu and X. Zhang, Appl. Phys. Lett. **103**, 141101 (2013).
28) J. B. Pendry, L. Martín-Moreno, and F. J. Garcia-Vidal, Science **305**, 847 (2004).
29) R. Wangberg, J. Elser, E. E. Narimanov, and V. A. Podolskiy, J. Opt. Soc. Am. B **23**, 498 (2006).
30) W. L. Barnes, J. Opt. A **8**, S87 (2006).
31) E. D. Palik, *Handbook of Optical Constants of Solids* (Elsevier, Amsterdam, 1985).
32) J. Lin, J. P. Balthasar Mueller, Q. Wang, G. Yuan, N. Antoniou, X.-C. Yuan, and F. Capasso, Science **340**, 331 (2013).
33) L. Yin, V. K. Vlasko-Vlasov, A. Rydh, J. Pearson, U. Welp, S.-H. Chang, S. K. Gray, G. C. Schatz, D. B. Brown, and C. W. Kimball, Appl. Phys. Lett. **85**, 467 (2004).